ACS NANO

www.acsnano.org

Article

Giant Photovoltaic Effect and Self-Powered Photodetection in Lateral MoS_2 Homojunctions via Strong Interface Coupling

Jiyuan Xu,[▽] Yinglun Sun,[▽] Gangqiang Zhou, Jiajun Fang, Alexei Barinov, Nitin Mallik, Azzedine Bendounan, Marino Marsi, Zailan Zhang,* Yingchun Cheng,* and Zhesheng Chen*

Cite This: *ACS Nano* 2026, 20, 5034−5043

Read Online

ACCESS | Metrics & More | Article Recommendations | Supporting Information

ABSTRACT: Lateral semiconductor homojunctions offer the advantages of perfect lattice matching and efficient carrier transport at the junctions, providing an ideal platform for high-performance optoelectronic devices. However, the fabrication of high-quality homostructures and the simultaneous realization of strong photovoltaic and photodetection performance remain challenging. In this work, we directly fabricated n^+-n^- MoS_2 homostructures, consisting of partly pristine MoS_2 and partly MoS_2 stacked on a CrOCl insulator. Efficient charge transfer occurs at the MoS_2/CrOCl interface, as confirmed by a ∼200 meV band shift observed in micro-ARPES measurements, consistent with our DFT calculations. As a result, the portion of MoS_2 stacked on CrOCl can be modulated to p-type by controlling the gate voltage, in sharp contrast to the pristine MoS_2 region. Moreover, the n^+-n^- MoS_2 homostructures exhibit an open-circuit voltage of 0.87 V, a detectivity exceeding 10^{12} Jones, and a responsivity of 0.98 A/W without external stimuli, demonstrating both ultrahigh photovoltaic and self-powered photodetection capabilities. The results presented in our work provide a strategy for developing efficient optoelectronic devices based on two-dimensional homostructures.

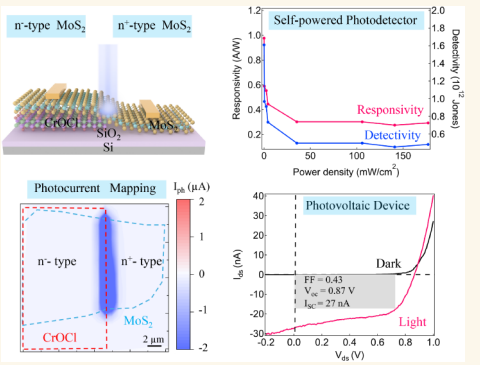

KEYWORDS: *homojunction, interlayer coupling, micro-ARPES, photovoltaic effect, photodetection*

1. INTRODUCTION

Two-dimensional (2D) van der Waals (vdW) layered materials provide an ideal platform for optoelectronic applications through symmetry-broken structures, such as distorted $MoTe_2$, or engineered interfaces, including 2D homostructures and heterostructures, which can induce strong internal electric fields and enhanced light−matter interactions.[1−4] In particular, 2D homojunctions formed within a single material are highly promising for optoelectronic devices, as they offer distinct advantages such as perfect lattice matching and efficient carrier diffusion across the junctions.[5−7] In this regard, heterojunctions often suffer from carrier scattering and trapping centers, which deteriorate charge transfer efficiency due to lattice mismatch and discontinuous band alignments.[8−12] However, unlike the fabrication of heterostructures, which typically requires only stacking different materials, the formation of homojunctions is considerably more challenging, as it necessitates precise and independent control of carrier doping in different regions of the same material.

In recent years, several strategies have been developed for fabricating 2D homojunctions, including split-gate modulation,[13] partial chemical doping,[14] partial photodoping,[15] and partial ferroelectric polarization.[16] Various types of homojunctions, such as p−n, n^+-n^-, and p^+-p^-, have been realized in different van der Waals layered materials.[17,18] The abrupt band bending at these homojunctions leads to a high built-in potential and efficient separation of photoexcited carriers. For example, improved rectifying characteristics and enhanced photoresponse have been achieved in 2D p−n homojunctions of semiconductors MoS_2[19] and black phosphorus[20] compared with their heterojunction counterparts. Nevertheless, most existing strategies for tuning carrier doping rely on precise control of carrier density by external stimuli. Therefore, identifying a simple yet effective method to modulate carrier concentration and achieve significant band bending at homojunction remains a critical challenge.

Interface coupling is an effective approach to modulate the properties of van der Waals materials through the proximity effect between adjacent layers.[21−23] Band hybridization or charge transfer at the interface can strongly modify the band structures or carrier concentrations of the individual materials. For example, a Berry curvature dipole and exotic nonlinear optoelectronic phenomena have been realized in symmetry-mismatched WSe_2/SiP heterointerfaces, arising from interfacial orbital hybridization.[24] In our recent studies, we observed a flat

Received: October 27, 2025
Revised: January 23, 2026
Accepted: January 23, 2026
Published: February 3, 2026

https://doi.org/10.1021/acsnano.5c18507
ACS Nano 2026, 20, 5034−5043

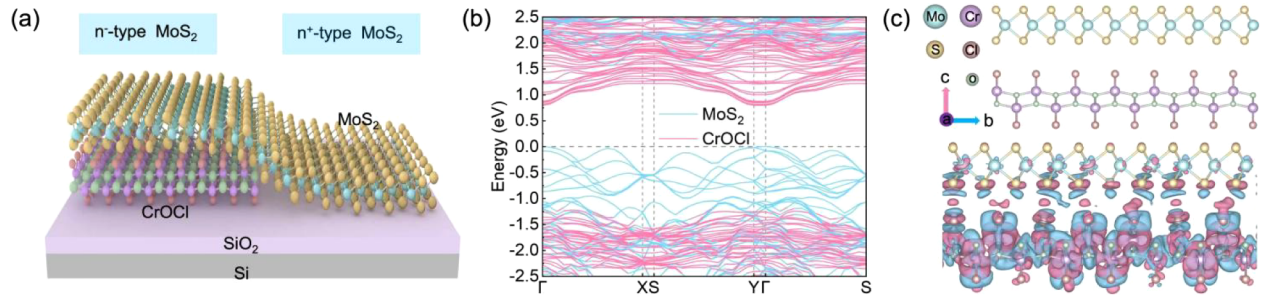

Figure 1. Schematic illustration of the lateral MoS_2 homojunction and the calculated interface coupling between MoS_2 and CrOCl. (a) Schematic of the lateral MoS_2 homojunction. (b) Calculated band structure of the MoS_2/CrOCl heterojunction. (c) Side view of the theoretical structural model (upper panel) and charge density difference (bottom panel) of the MoS_2/CrOCl heterostructure, where charge accumulation and depletion are shown in red and blue, respectively.

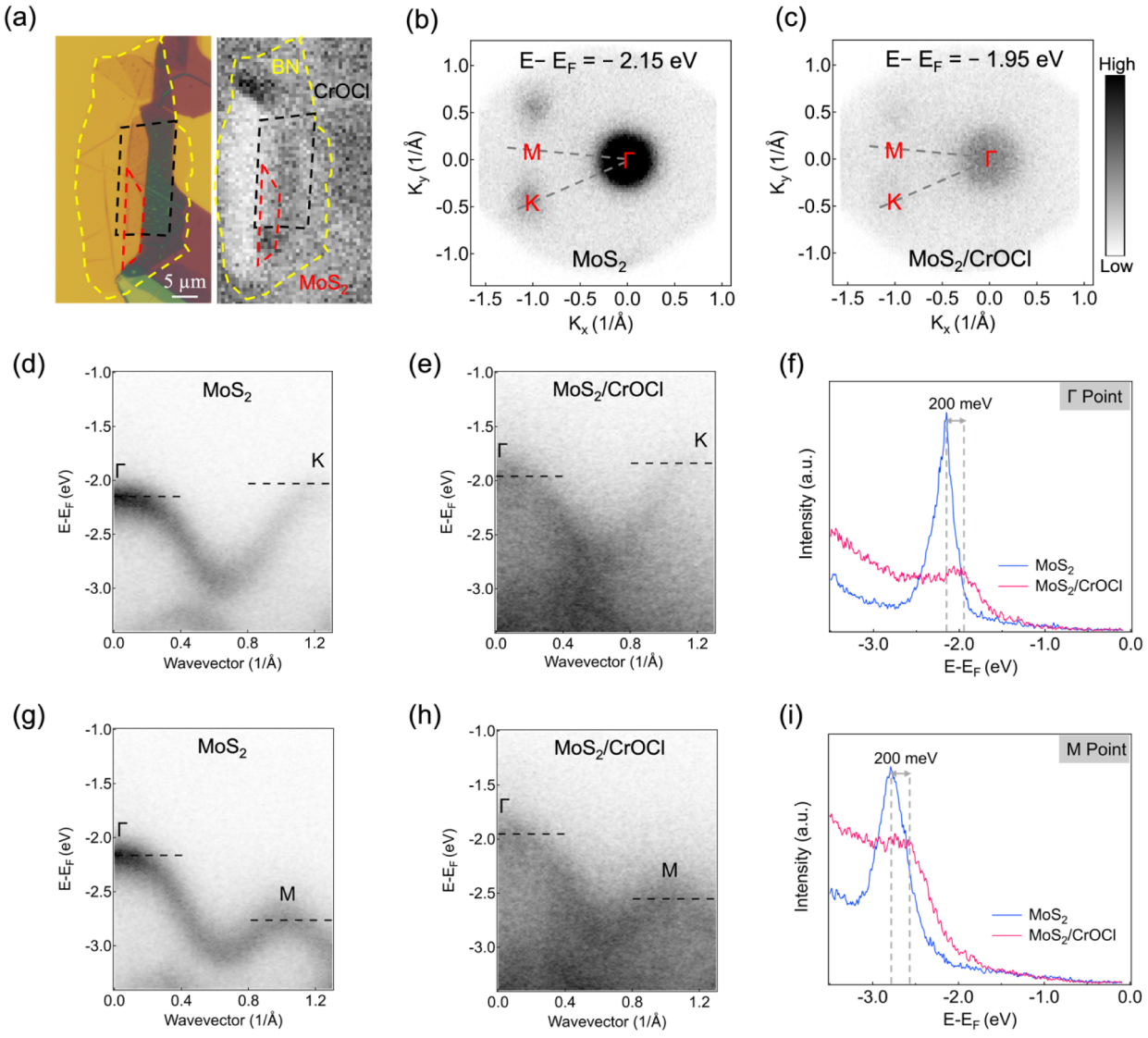

Figure 2. Band structures of pristine $MoS_2$and the MoS_2/CrOCl heterostructure. (a) Optical image and corresponding SPEM map. The monolayer MoS_2, few-layer CrOCl, and BN regions are outlined by red, black, and yellow dashed curves, respectively. The scale bar corresponds to 5 μm. (b, c) Constant-energy cut from the 3D ARPES map of (b) pristine MoS_2 at $E - E_F = -2.15$ eV and (c) the MoS_2/CrOCl heterostructure at $E - E_F = -1.95$ eV. (d, e) Band dispersions of (d) pristine MoS_2 and (e) MoS_2/CrOCl along the $\Gamma-K$ directions. (f) EDCs extracted from the Γ points of pristine MoS_2 and MoS_2/CrOCl. (g, h) Band dispersions of (g) pristine MoS_2 and (h) MoS_2/CrOCl along the $\Gamma-M$ directions. (i) EDCs extracted from the M points of pristine MoS_2 and MoS_2/CrOCl.

band and broken rotational symmetry in monolayer MoS_2 when it was stacked on black phosphorus, arising from strong hybridization between Mo d_{z^2} and P p_x orbitals.[25] In addition, we directly observed giant charge transfer between MoS_2 and

https://doi.org/10.1021/acsnano.5c18507
ACS Nano 2026, 20, 5034−5043

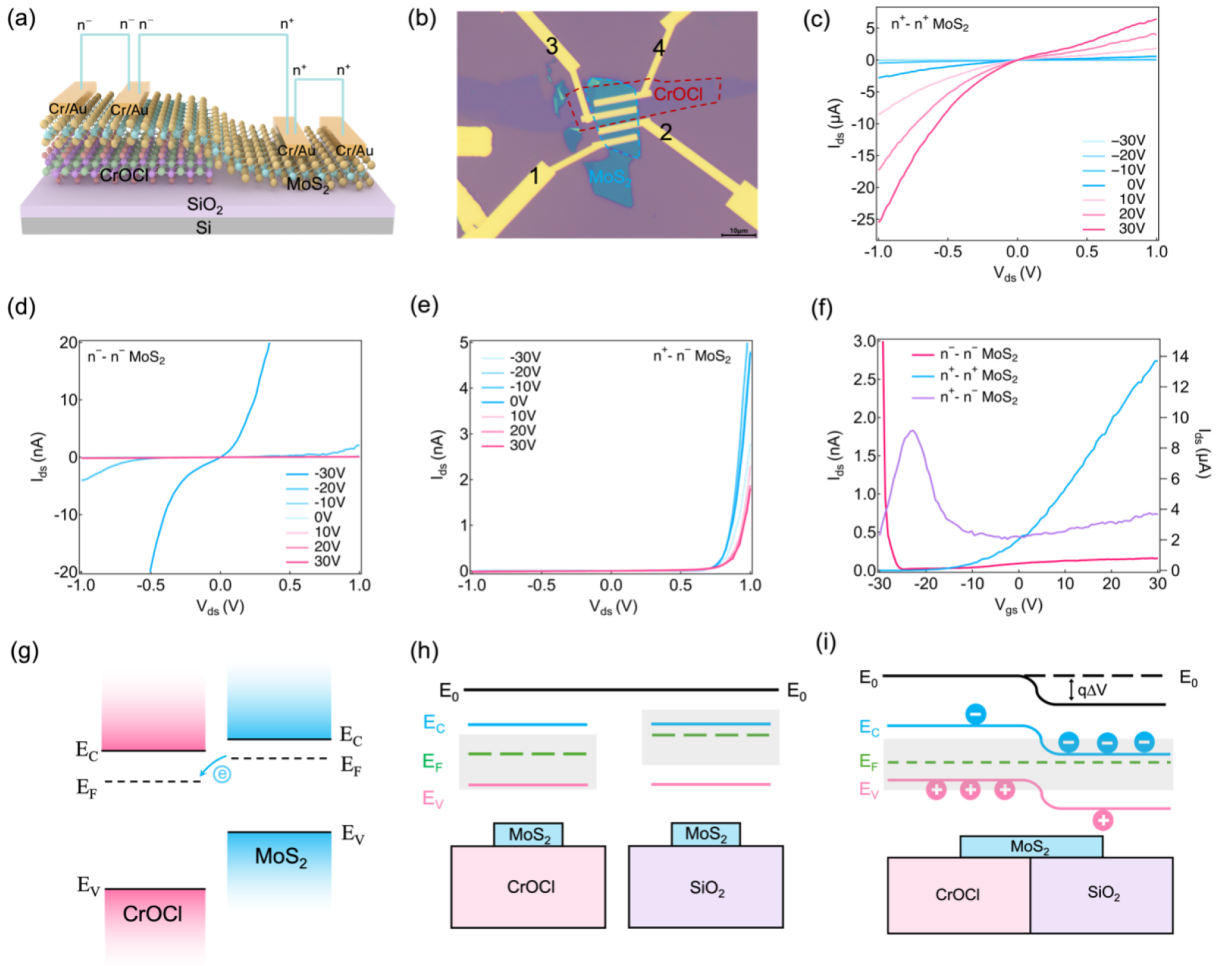

Figure 3. FET performance based on the lateral MoS_2homojunction. (a) Schematic diagrams of n^+−n^+, n^-−n^-, and n^+−n^- FETs based on MoS_2. (b) Optical image of the fabricated FET devices. (c) I_{ds}−V_{ds} curves of the n^+−n^+ MoS_2 FET at different gate voltages. (d) I_{ds}−V_{ds} curves of the n^-−n^- MoS_2 FET at different gate voltages. (e) I_{ds}−V_{ds} curves of the n^+−n^- MoS_2 FET at different gate voltages. (f) Transfer characteristics of the FETs measured at V_{ds} = 1 V. (g) Band diagrams of MoS_2 and CrOCl before contact. (h) Band diagrams of pristine MoS_2 and MoS_2 stacked on CrOCl. (i) Band diagram of the lateral n^+−n^- MoS_2 homojunction.

TiS_3 semiconductors, enabling the realization of a photovoltaic polarity-switching photodetector.[26]

In principle, a semiconductor homostructure can be constructed from the pristine material together with the pristine semiconductor stacked on interface-coupled materials. However, it is important to emphasize that the interface-coupled materials should ideally be insulators, so as not to interfere with the transport properties of the semiconductor homojunction.[27] CrOCl is a recently reported stable 2D vdW magnetic insulator with an anisotropic structure and a large band gap of ∼2.8 eV in its bulk form.[28,29] Moreover, it exhibits strong interlayer coupling with transition metal dichalcogenide (TMD) semiconductors. For example, transitions from isotropic to anisotropic properties, as well as from n-type to p-type behavior in MoS_2, have been reported due to interlayer coupling at the TMD/CrOCl interface.[30−32] However, the applications of TMD/CrOCl heterostructures in optoelectronic devices have not yet been explored, despite their potential for high performance owing to the strong charge transfer that can be induced at the interface.

In this work, as a proof of concept, we fabricated lateral n^+−n^- MoS_2 homojunctions by combining pristine MoS_2 and MoS_2 coupled with CrOCl. The charge transfer and band shifts of MoS_2 at the MoS_2/CrOCl interface were directly observed using micro-angle-resolved photoemission spectroscopy (micro-ARPES). Notably, field-effect transistors (FETs) exhibit n-type behavior in pristine MoS_2, p-type behavior in MoS_2/CrOCl, and antiambipolar characteristics in the homojunction under gate voltage modulation. Furthermore, optoelectronic devices based on the MoS_2 homojunction demonstrate both a giant photovoltaic effect and efficient photodetection, with an open-circuit voltage up to 0.87 V and a responsivity of up to 0.98 A/W under self-powered operation, representing the highest performance among TMD-based optoelectronic devices. Our findings on lateral MoS_2 homojunctions not only establish an efficient route for constructing lateral semiconductor homojunctions, but also open up opportunities for high-performance optoelectronic devices capable of operating in both photovoltaic and photodetection modes.

2. RESULTS AND DISCUSSION

To achieve the lateral MoS_2 homostructure, we proposed a design in which one-half of the MoS_2 remains in its pristine form, exhibiting strong n-type doping (n^+), while the other half is placed on CrOCl. Previous studies have shown that CrOCl

https://doi.org/10.1021/acsnano.5c18507
ACS Nano 2026, 20, 5034−5043

can extract electrons from MoS_2, thereby reducing its electron concentration and making it less n-type (n^-). The schematic of this lateral MoS_2 homostructure is shown in Figure 1a. To investigate the interlayer coupling between MoS_2 and CrOCl, the band structure and charge density difference were calculated using density functional theory (DFT). As shown in Figure 1b, the conduction band minimum (CBM) of CrOCl is 0.77 eV lower than that of MoS_2, while the valence band maximum (VBM) of CrOCl is also 1.17 eV lower, indicating a type-II band alignment. The theoretical structural model and charge density difference at the MoS_2/CrOCl interface are presented in Figure 1c. The charge density difference map shown in the bottom panel reveals that electrons transfer from S atoms in MoS_2 near the interface to Cl atoms in CrOCl. In addition, the band structures of the individual monolayer MoS_2 and CrOCl, the density of states (DOS) with different orbital contributions for the MoS_2/CrOCl heterostructure and the plane-averaged charge density difference of the MoS_2/CrOCl heterostructure along the Z direction are further presented in Figures S1−S3. These results indicate that electrons can be effectively transferred from the MoS_2 layer to the CrOCl layer, reducing the n-type doping level of MoS_2, which is consistent with previous findings.

To investigate the band shift in MoS_2 induced by interfacial coupling, we performed micro-ARPES measurements on a MoS_2/CrOCl heterostructure. The charge transfer at the MoS_2/CrOCl interface can lead to a shift in the MoS_2 band structure due to interlayer coupling. The samples were fabricated using the dry-transfer method, as described in our previous work (see the Experimental Section). In this heterostructure, the MoS_2/BN region represents pristine MoS_2, where no charge transfer occurs at the interface, while the MoS_2/CrOCl region represents the coupled heterostructure. The micro-ARPES measurements were carried out at the Spectromicroscopy beamline of the Elettra Synchrotron Light Source in Italy, using a photon energy of $h\nu$ = 74 eV under room temperature (see the Experimental Section). The optical image and corresponding scanning photoemission microscopy (SPEM) image are shown in Figure 2a. The pristine MoS_2 and MoS_2/CrOCl regions can be clearly distinguished by the photoemission signal contrast in the SPEM image. Furthermore, the high-symmetry directions of MoS_2 were determined from constant energy cuts of the 3D ARPES maps acquired in both the pristine MoS_2 and the MoS_2/CrOCl heterostructure regions, as shown in Figure 2b,c. The Γ−K and Γ−M directions are labeled in the constant-energy cuts for pristine MoS_2 and the heterostructure. The corresponding band dispersions along these two directions are presented in Figure 2d,g. In pristine MoS_2, the VBM is located at the K point at $E - E_F \approx -2.0$ eV, even though the photoemission intensity is weaker than at the Γ point. The position of the VBM confirms that the pristine MoS_2 is monolayer and strongly n-doped. In contrast, the band dispersion of MoS_2 stacked on CrOCl exhibits a rigid energy shift, indicating a reduction in n-type doping of MoS_2 due to charge transfer to CrOCl as shown in Figure 2e,h.

It is worth noting that the CrOCl bands are not clearly resolved in the ARPES spectra. This is mainly because the ARPES signals detected using a photon energy of 74 eV originate exclusively from the extreme surface region of the sample, within approximately ∼5 Å, whereas monolayer MoS_2 has a thickness of ∼6 Å (S−Mo−S atomic structure), which slightly exceeds the inelastic mean free path of photoexcited electrons. Consequently, the band structure signal from the material underneath the monolayer MoS_2 is strongly suppressed. This absence of subsurface band features is consistent with our previous observations in MoS_2/bP and MoS_2/TiS_3 heterostructures.[25,26] To quantify the band shift in MoS_2, energy distribution curves (EDCs) were extracted at the Γ and M points, as shown in Figure 2f,i. The EDCs at the Γ point reveal a photoemission peak shift of approximately 200 meV, consistent with the energy shift at the M point. This rigid band shift in MoS_2 demonstrates strong interfacial coupling between MoS_2 and CrOCl, confirming that a lateral n^+−n^- MoS_2 homostructure can be achieved simply by stacking the layers in the desired regions.

The schematic of a lateral-channel field-effect transistor (FET) based on few-layer MoS_2 coupled with CrOCl is illustrated in Figure 3a. The optical image of the fabricated FET device is shown in Figure 3b (see the Experimental Section for details of the device fabrication process). The FET device consists of three distinct channels for carrier transport: an n^+−n^+ FET on pristine MoS_2 (contacts 1 and 2), an n^-−n^- FET on MoS_2 stacked on CrOCl (contacts 3 and 4), and an n^+−n^- FET bridging the pristine MoS_2 and MoS_2/CrOCl regions (contacts 2 and 3). Prior to electrical measurements, Raman, photoluminescence (PL), and atomic force microscopy (AFM) characterizations were performed to assess the sample quality, as shown in Figures S4−S7. In the Raman spectra, the peaks of pristine MoS_2 at 383 and 408 cm^{-1} correspond to the in-plane (E^1_{2g}) and out-of-plane (A^1_g) vibration modes, respectively. For CrOCl, the characteristic peaks at 206, 416, and 455 cm^{-1} are attributed to the out-of-plane A^1_g, A^2_g, and A^3_g modes, respectively. Notably, the A^1_g mode frequency of MoS_2 in the heterostructure exhibits a blue shift relative to that of pristine MoS_2, which may arise from strain effects or carrier doping in MoS_2.[33,34] In the PL spectra, the PL intensity of MoS_2/CrOCl is significantly lower than that of pristine MoS_2, indicating strong PL quenching. This observation further confirms efficient interlayer charge transfer at the MoS_2/CrOCl interface. The thicknesses of the materials were determined by AFM to be approximately 9.0 nm for MoS_2 and 4.4 nm for CrOCl, respectively. It is also worth noting that both CrOCl and MoS_2 exhibit excellent stability under ambient conditions, as evidenced by their Raman spectra after several days of exposure to air, which is critical for practical device applications.

The source−drain current (I_{ds}) as a function of source−drain voltage (V_{ds}) under different gate voltages (V_{gs}) for the three types of FETs is presented in Figure 3c−e. For both the n^+−n^+ MoS_2 and n^-−n^- MoS_2 FETs, the I_{ds}−V_{ds} curves exhibit slightly nonlinear behavior, consistent with previous reports.[35,36] The current in the n^-−n^- MoS_2 device shown in Figure 3c is much lower than that in the n^+−n^+ MoS_2 device shown in Figure 3d, confirming the reduced n-type doping level in MoS_2 on CrOCl. In contrast, the n^+−n^- MoS_2 device displays a pronounced rectifying behavior in the I_{ds}−V_{ds} characteristics, indicative of asymmetric carrier transport across the lateral junction. Furthermore, the transfer characteristics (I_{ds}−V_{gs} curves) exhibit distinct behaviors for the three devices when tuning V_{gs} at V_{ds} = 1 V, as shown in Figure 3f. In the n^+−n^+ MoS_2 FET, the current increases smoothly with increasing V_{gs}, characteristic of an n-type transistor. In contrast, the n^-−n^- MoS_2 FET shows a sharp increase in current with decreasing V_{gs} from −20 V, typical of a p-type transistor. We

https://doi.org/10.1021/acsnano.5c18507
ACS Nano 2026, 20, 5034−5043

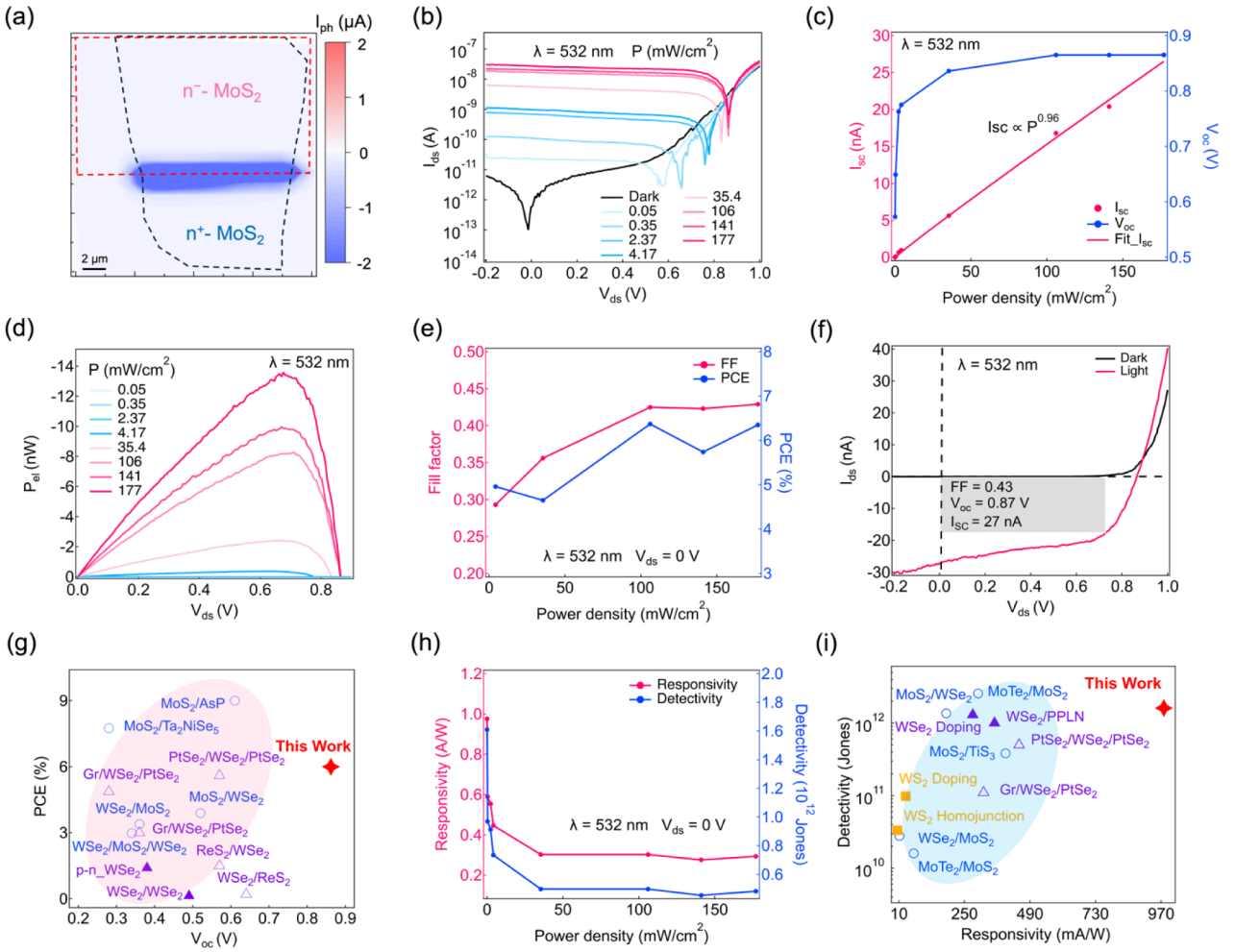

Figure 4. Optoelectronic characterization of the lateral n^+−n^- MoS_2homojunction under 532 nm illumination. (a) Photocurrent mapping under self-powered operation. (b) I_{ds}−V_{ds} curves measured at different illumination power densities. (c) V_{oc} and I_{sc} as functions of illumination power density. (d) Output power of the device as a function of V_{ds} at different illumination power densities. (e) FF and PCE as functions of illumination power density. (f) Photovoltaic performance of the device under an illumination power density of 177 mW/cm². (g) Comparison of PCE and V_{oc} with previously reported 2D photovoltaic devices.[40−51] (h) Responsivity and detectivity as functions of illumination power density. (i) Comparison of detectivity and responsivity with other photodetectors based on TMD heterostructures.[16,26,41−43,52−57]

refer to the device as a p-type transistor here only because the Fermi level can be shifted toward the valence band maximum under the application of a large negative gate voltage, which is not in conflict with the original n^- type of MoS_2 on CrOCl in the absence of a gate voltage. Interestingly, the n^+−n^- MoS_2 FET exhibits antiambipolar behavior, where the current first increases and then decreases as a function of V_{gs}, reflecting the formation of a lateral n^+−n^- homojunction within the MoS_2 channel. It is worth noting that the in-plane conductivity of CrOCl is extremely low and does not contribute to the transport properties of the n^+−n^- MoS_2 homojunction. As shown in Figure S8, for an isolated CrOCl flake, the current is on the order of 1 pA even under a high source−drain voltage of 5 V, and negligible photocurrent is generated. This value is several orders of magnitude smaller than the typical channel current measured in our MoS_2 homojunction devices. Moreover, the drain current remains in the pA range even after applying a gate voltage of 60 V. This direct comparison provides conclusive experimental evidence that the lateral current measured in our main devices originates exclusively from the MoS_2 homojunction, with negligible contribution from the CrOCl substrate.

Based on our experimental results and previous studies, it is well established that electrons can be transferred from MoS_2 to CrOCl, and that the work function of CrOCl is higher than that of MoS_2.[30,37] The energy band diagram of the MoS_2/CrOCl heterostructure before contact is shown in Figure 3g. The band diagram of the lateral n^+−n^- homojunction is further analyzed, as shown in Figure 3h,i. As pristine MoS_2 is highly n-doped, as confirmed by the micro-ARPES results, the band diagram of pristine MoS_2 and the corresponding Fermi level modulation region induced by the gate voltage are illustrated in the right panel of Figure 3h. For MoS_2 stacked on CrOCl, the Fermi level of MoS_2 is initially adjusted due to charge transfer from MoS_2 to CrOCl, as evidenced by the rigid band shift observed in the micro-ARPES measurements. Moreover, according to the FET characteristics of MoS_2 on CrOCl, the gate voltage can further modulate the Fermi level toward the VBM, and the associated modulation region is shown in the left panel of Figure 3h. In the lateral n^+−n^- MoS_2 homojunction, band bending occurs at the junction between the n^+ and n^- regions of MoS_2, as the Fermi levels must align through carrier diffusion and drift, as shown in Figure 3i. A built-in potential ($q\Delta V$) is established at the junction under

https://doi.org/10.1021/acsnano.5c18507
ACS Nano 2026, 20, 5034−5043

equilibrium conditions. Owing to this significant built-in potential, the n^+-n^- MoS_2 homojunction holds great potential for applications in photovoltaic and photodetection devices.

In the following, the photovoltaic and photodetection performance of the lateral n^+-n^- MoS_2 homojunction are investigated. Photocurrent mapping was first performed under 532 nm laser illumination at self-powered operation mode, as shown in Figure 4a. The results clearly indicate that the photocurrent is generated exclusively at the homojunction, highlighting the dominant contribution of the homojunction rather than the MoS_2–Au metal–semiconductor contacts. This confirms that the built-in electric field formed at the n^+-n^- junction plays a key role in charge carrier separation and photocurrent generation. Raman mapping of the same region is presented in Figure S9 for comparison with the photocurrent generation area. In addition, the $I_{ds}-V_{ds}$ characteristics measured under different illumination power densities are shown in Figure 4b. The dark current at V_{ds} = 0 V was measured to be ~100 fA, which is the detection limit of the measurement setup. Under illumination with a power density of 0.05 mW/cm^2, the current increases by nearly 2 orders of magnitude, and the minimum point of the curve exhibits a significant shift, indicating a pronounced photovoltaic effect in the lateral n^+-n^- MoS_2 homojunction.

The photovoltaic performance was evaluated using the key figures of merit: short-circuit current (I_{sc}), open-circuit voltage (V_{oc}), fill factor (FF), and power conversion efficiency (PCE). The I_{sc} increase with illumination power density, following power-law behavior $I_{sc} \propto P^{\alpha}$ ($\alpha \approx 0.96$), and the V_{oc} follows $V_{oc} \propto \log(P)$, as shown in Figure 4c. The near-unity power factor α suggests that the photovoltaic effect dominates carrier transport. After illumination, the photogenerated carrier density increases proportionally with power density, leading to a larger quasi-Fermi level separation and consequently an increased V_{oc}. The FF is defined as FF = $P_{max}/(V_{oc}I_{sc})$, where P_{max} represents the maximum output power. The output power as a function of V_{ds} at different illumination power densities is shown in Figure 4d, from which P_{max} is extracted at the peak position. The PCE is defined as PCE = $V_{oc}I_{sc}FF/P_{in}$, where P_{in} is the incident illumination power density. The FF and PCE calculated at different power densities are presented in Figure 4e, both showing a gradual increase with increasing illumination intensity. At an illumination power density of 177 mW/cm^2, the photovoltaic device exhibits a V_{oc} of 0.87 V, an I_{sc} of −27 nA, an FF of 0.43, and a PCE of up to 6.35%. The corresponding $I_{ds}-V_{ds}$ curves under dark and illuminated conditions are shown in Figure 4f. Furthermore, a comparison of V_{oc} and PCE with other TMD-based photovoltaic devices is presented in Figure 4g. It is evident that the V_{oc} achieved in the lateral n^+-n^- MoS_2 homojunction is significantly higher, originating from the efficient photoexcited charge separation driven by the strong built-in potential, as well as the enhanced carrier transport resulting from reduced carrier scattering within the homojunction compared to conventional heterojunction interfaces. It is noteworthy that no photovoltaic response (neither I_{sc} nor V_{oc}) is observed in either the n^+-n^+ or n^--n^- MoS_2 FETs, as shown in Figure S10, further confirming that the homojunction is responsible for the photovoltaic effect, consistent with the photocurrent mapping results.

At self-powered operation mode, the photodetection performance of the lateral n^+-n^- MoS_2 homojunction was further investigated. The key figures of merit, namely the responsivity (R) and specific detectivity (D^*), were extracted as functions of illumination power density, as shown in Figure 4h. R is defined as $R = I_{ph}/P_{in}$, and D^* is calculated using the dark current method, $D^* = A^{1/2}R/(2eI_{dark})^{1/2}$, where A denotes the effective device area. Both R and D^* increase with decreasing illumination power density. Under 532 nm illumination with a power intensity of 0.05 mW/cm^2, the device achieves a high responsivity of 0.98 A/W and a detectivity of 1.61×10^{12} Jones. A comparison of R and D^* for the lateral n^+-n^- MoS_2 homojunction with other self-powered photodetectors based on TMD materials is shown in Figure 4i. It is evident that both R and D^* in our device are among the highest reported values, demonstrating its outstanding performance in the field of self-powered photodetection.

The transient photoresponse as a function of illumination power, the rise and fall times of the photocurrent, and the long-term stability of the photoresponse are characterized in Figures S11–S12. The photocurrent rapidly increases and stabilizes when the laser is switched on and promptly returns to its initial state when the laser is switched off. This fast and reproducible switching behavior over multiple cycles confirms that the photocurrent originates from photogenerated carriers rather than laser-induced heating effects. The measured rise and fall times are 35 and 29 μs, respectively, demonstrating the device's capability for high-speed photodetection. Remarkably, the device retains more than 97% of its initial photocurrent after 30 days of storage in ambient air, indicating exceptional robustness. In addition, the reproducibility of this high performance is confirmed across multiple devices. For example, the performance of another n^+-n^- MoS_2 homojunction device is shown in Figure S13. This device exhibits an identical rectifying $I-V$ characteristic and a self-powered photovoltaic response, providing direct and compelling evidence that the observed effect is intrinsic to the MoS_2/CrOCl interface. A simple imaging demonstration based on the lateral n^+-n^- MoS_2 homojunction device was also performed, as shown in Figure S14. The resulting image of the pattern "NJUST" exhibits excellent clarity and precision, indicating high spatial resolution. In addition, the photovoltaic and photodetection characteristics of the same device under 635 nm illumination were further measured, as shown in Figure S15. It is evident that the device exhibits robust and consistent performance under both 532 and 635 nm illumination, which is significantly superior to that of many previously reported TMD-based devices. Importantly, this substrate-induced doping approach inherently avoids complex chemical processes and could be compatible with large-area van der Waals material transfer techniques, suggesting promising pathways toward scalable device integration despite current fabrication-scale limitations. In addition to the enhancement of light–matter interactions through interface coupling, other emerging material-engineering strategies have also been developed simultaneously.[38,39] For example, super-resolution nanogroove array (NGA) structures have been fabricated in 2D multilayer $NbOI_2$ using a controlled nanoscale modification approach based on far-field femtosecond laser patterning, and the resulting NGA-$NbOI_2$ gas sensors exhibit excellent NO_2 sensing performance with a rapid response time.[39] Looking ahead, it will be essential to integrate these advanced strategies in a controlled manner to achieve further optical enhancement and to enable high-performance optoelectronic device applications.

https://doi.org/10.1021/acsnano.5c18507
ACS Nano 2026, 20, 5034–5043

3. CONCLUSION

In conclusion, for the first time, we have demonstrated outstanding optoelectronic properties in a lateral MoS_2 homojunction fabricated simply by integrating pristine MoS_2 with MoS_2 stacked on a CrOCl insulator. Benefiting from charge transfer from MoS_2 to CrOCl, the MoS_2/CrOCl region exhibits a ∼200 meV band shift and reduced electron doping, as confirmed by both DFT calculation and micro-ARPES measurements. The resulting lateral n^+-n^- MoS_2 homojunction simultaneously delivers ultrahigh photovoltaic and photodetection performance, achieving a V_{oc} of up to 0.87 V and a responsivity approaching 1 A/W under self-powered operation, among the highest values reported for TMD-based optoelectronic devices. Our results establish a universal strategy not only for constructing lateral semiconductor homojunctions with perfect lattice matching and efficient carrier transport, but also for developing high-performance, multifunctional devices that integrate efficient photovoltaic conversion and self-powered photodetection within a single van der Waals semiconductor platform.

4. EXPERIMENTAL SECTION

4.1. Theoretical Calculation

All first-principles calculations in this work were performed by using DS-PAW package, in which the Perdew−Burke−Ernzerhof (PBE) functional of the generalized gradient approximation (GGA) was adopted for electron exchange and correlation interactions.[58] To better describe the strong correlation effects of d-orbital electrons in Cr atoms, the DFT + U method was employed with the U value of 3 eV.[59] The primitive cell of CrOCl is orthorhombic, with optimized lattice constants of a = 3.23 Å and b = 3.92 Å. The primitive cell of MoS_2 is hexagonal, with optimized lattice constants of $a = b$ = 3.20 Å. To build the CrOCl/MoS_2 heterostructure, an orthorhombic unit cell of MoS_2 was built and the lattice constants are a = 3.20 Å, b = 5.54 Å. A 1 × 7 supercell for the CrOCl and a 1 × 5 supercell for orthorhombic MoS_2 were adopted. The CrOCl supercell with lattice constant a = 3.23 Å, b = 27.44 Å and MoS_2 supercell with lattice constant a = 3.20 Å, b = 27.70 Å are obtained. The lattice constants of the MoS_2 supercell were chosen as the lattice constant of the heterostructure. A vacuum spacing greater than 15 Å was employed. The structure was optimized until the largest force on each atom was less than 0.01 eV/Å. The lattice mismatch rate between CrOCl and MoS_2 is less than 5%, which is acceptable. The cutoff energy was set to 550 eV, and a 2 × 2 × 1 Monkhorst−Pack k-mesh was used for sampling the Brillouin zone of CrOCl/MoS_2 heterostructure.[60] The van der Waals interactions between layers were corrected using the DFT-D3 functional.[61]

4.2. Sample and Device Fabrication

Multilayer BN, multilayer CrOCl, and monolayer or few-layer MoS_2 flakes were first exfoliated onto separate SiO_2/Si substrates under ambient conditions. The MoS_2/CrOCl heterostructures were then assembled by partially stacking the flakes with high precision under an optical microscope. Briefly, MoS_2 was first picked up using a polycarbonate (PC) film supported on a polydimethylsiloxane (PDMS) stamp. The CrOCl flake on the SiO_2/Si substrate was then aligned and brought into contact with the PDMS−PC−MoS_2 stack, followed by peeling off to form a half PDMS−PC−MoS_2 and half PDMS−PC−MoS_2/CrOCl structure. For micro-ARPES measurements, an additional BN flake was subsequently transferred onto the PDMS−PC−MoS_2 and PDMS−PC−MoS_2/CrOCl regions using the same approach, and the entire stack was finally placed on an Au/SiO_2/Si substrate. For optoelectronic device fabrication, the half PDMS−PC−MoS_2 and half PDMS−PC−MoS_2/CrOCl structure was instead directly transferred onto a SiO_2/Si substrate. After transfer, the PDMS stamp was smoothly peeled off following a mild heating process at ∼180 °C. The PC film was then removed by immersing the sample in chloroform and drying it inside the glovebox. Finally, for the lateral n^+-n^- MoS_2 homojunction device, electron-beam lithography followed by 3 nm/50 nm Cr/Au metal deposition was performed to define the electrodes.

4.3. Micro-ARPES Experiment

Micro-ARPES measurements of MoS_2/CrOCl heterostructures were performed at the Spectromicroscopy beamline of the Elettra light source in Italy. In order to clean the sample surface, the samples were annealed at ∼350 °C for 10 h in the preparation chamber under ultrahigh vacuum before micro-ARPES experiments. The pressure in the experimental chamber was better than 1×10^{-10} mbar during micro-ARPES measurements. At Spectromicroscopy beamline, linearly p-polarized light with a fixed incident angle of 45° was focused to ∼600 nm by Schwarzschild objective. All the experiments were performed at room temperature with photon energy of $h\nu$ = 74 eV. The overall energy and momentum resolution of the experiment was ∼45 meV and 0.005 $Å^{-1}$.

4.4. Optical Spectroscopy and Device Characterization

Raman and photoluminescence spectra, along with their corresponding spatial mappings, were obtained using a 532 nm (Aramis, Horiba Jobin Yvon). The photodetection characteristics of the devices were measured using a semiconductor device parameter analyzer (Keysight B1500A), with 532 and 635 nm diode lasers serving as the light sources. Laser power was calibrated with a light power meter (Newport, Model 2936-R). For photocurrent mapping and polarization photodetection imaging, a motorized X−Y stage was used to scan the devices under a 532 nm laser focused using a 50× objective lens. The diameter of the laser spot is approximately 1 μm.

■ ASSOCIATED CONTENT

Data Availability Statement

The data that support the findings of this study are available from the corresponding author upon reasonable request.

Supporting Information

The Supporting Information is available free of charge at https://pubs.acs.org/doi/10.1021/acsnano.5c18507.

Band structures of MoS_2 and CrOCl; orbital-resolved density of states; plane-averaged charge density difference; Raman spectra; environmental stability of CrOCl and MoS_2/CrOCl; photoluminescence spectra; AFM characterization; optoelectronic characterization of the CrOCl device; Raman mapping of the MoS_2/CrOCl heterojunction; $I_{ds}-V_{ds}$ characterization of n^+-n^+ MoS_2 and n^-n^- MoS_2 devices as a function of light intensity; dynamic photoresponse performance; long-term operational stability of the homojunction photodetector; optoelectronic characterization of an additional lateral n^+-n^- MoS_2 homojunction device; self-powered imaging; and optoelectronic characterization of the homojunction device under 635 nm illumination (PDF)

■ AUTHOR INFORMATION

Corresponding Authors

Zhesheng Chen − *School of Material Science and Engineering, Nanjing University of Science and Technology, Nanjing 210094, P. R. China;* orcid.org/0000-0001-7978-5637; Email: zhesheng.chen@njust.edu.cn

Zailan Zhang − *School of Physics, Nanjing University of Science and Technology, Nanjing 210094, P. R. China;* Email: zhangzailan@njust.edu.cn

Yingchun Cheng − *State Key Laboratory of Metastable Materials Science & Technology and Key Laboratory for Microstructural Material Physics of Hebei Province, School of*

https://doi.org/10.1021/acsnano.5c18507
ACS Nano 2026, 20, 5034−5043

Science, Yanshan University, Qinhuangdao 066004, P. R. China; orcid.org/0000-0002-8495-9184;
Email: iamyccheng@ysu.edu.cn

Authors

Jiyuan Xu − *School of Material Science and Engineering, Nanjing University of Science and Technology, Nanjing 210094, P. R. China*

Yinglun Sun − *State Key Laboratory of Metastable Materials Science & Technology and Key Laboratory for Microstructural Material Physics of Hebei Province, School of Science, Yanshan University, Qinhuangdao 066004, P. R. China*

Gangqiang Zhou − *School of Material Science and Engineering, Nanjing University of Science and Technology, Nanjing 210094, P. R. China*

Jiajun Fang − *School of Material Science and Engineering, Nanjing University of Science and Technology, Nanjing 210094, P. R. China*

Alexei Barinov − *Elettra-Sincrotrone Trieste SCpA, Trieste 34149, Italy*

Nitin Mallik − *Société Civile Synchrotron Soleil, Saint-Aubin 91190, France;* orcid.org/0000-0003-2167-1711

Azzedine Bendounan − *Société Civile Synchrotron Soleil, Saint-Aubin 91190, France;* orcid.org/0000-0001-7557-4322

Marino Marsi − *Université Paris-Saclay, CNRS, Laboratoire de Physique des Solides, Orsay 91405, France;* orcid.org/0000-0002-4335-3637

Complete contact information is available at: https://pubs.acs.org/10.1021/acsnano.5c18507

Author Contributions

[▽]J.X. and Y.S. contributed equally. Z.C. and Z.Z. supervised the project. J.X. fabricated all heterostructures and devices with the help of G.Z. and J.F. J.X. performed all optoelectronic measurements. Y.S. conducted the DFT calculations and grew CrOCl single crystals under the supervision of Y.C. N.M., A.B., M.M., and Z.C. performed the micro-ARPES experiments at the Elettra light source. A.B. was responsible for the Spectromicroscopy beamline at the Elettra light source. J.X., Z.Z., and Z.C. analyzed the experimental data and wrote the manuscript with contributions from all other authors.

Notes

The authors declare no competing financial interest.

■ ACKNOWLEDGMENTS

This work was financially supported by the National Natural Science Foundation of China (grant nos. 12574075 and 62274087), the Natural Science Foundation of Jiangsu Province (grant no. BK20252041), and the Nanjing University of Science and Technology (grant nos. AE899991/406 and AD411203). We thank the Elettra light source for the provision of micro-ARPES beamtime under proposal no. 20245436.

■ REFERENCES

(1) Aftab, S.; Shehzad, M. A.; Salman Ajmal, H. M.; Kabir, F.; Iqbal, M. Z.; Al-Kahtani, A. A. Bulk Photovoltaic Effect in Two-Dimensional Distorted $MoTe_2$. *ACS Nano* **2023**, *17* (18), 17884−17896.

(2) Lee, D.; Lee, J. J.; Kim, Y. S.; Kim, Y. H.; Kim, J. C.; Huh, W.; Lee, J.; Park, S.; Jeong, H. Y.; Kim, Y. D.; Lee, C.-H. Remote Modulation Doping in van der Waals Heterostructure Transistors. *Nat. Electron.* **2021**, *4* (9), 664−670.

(3) Zhou, G.; Xu, J.; Wang, Z.; Mallik, N.; Bendounan, A.; Zhang, Z.; Chen, Z. Anisotropic $PdSe_2$/GeAs Heterostructures with Switchable Photocurrent Polarity for Polarization Imaging and Programmable Logic Gates. *Small* **2026**, No. e11859.

(4) Muhammad Salman Ajmal, H.; Muneer, R.; Saeed, A.; Tanveer, M.; Ahsan Saeed, M. Synergistic Role of Green-Synthesized Zinc Oxide Nanomaterials in Biomedicine Applications. *ChemistrySelect* **2024**, *9* (36), No. e202402517.

(5) Utama, M. I. B.; Kleemann, H.; Zhao, W.; Ong, C. S.; Da Jornada, F. H.; Qiu, D. Y.; Cai, H.; Li, H.; Kou, R.; Zhao, S.; Wang, S.; Watanabe, K.; Taniguchi, T.; Tongay, S.; Zettl, A.; Louie, S. G.; Wang, F. A Dielectric-Defined Lateral Heterojunction in a Monolayer Semiconductor. *Nat. Electron.* **2019**, *2* (2), 60−65.

(6) Li, D.; Chen, M.; Sun, Z.; Yu, P.; Liu, Z.; Ajayan, P. M.; Zhang, Z. Two-Dimensional Non-Volatile Programmable p−n Junctions. *Nat. Nanotechnol.* **2017**, *12* (9), 901−906.

(7) Wang, G.; Zhang, M.; Chen, D.; Guo, Q.; Feng, X.; Niu, T.; Liu, X.; Li, A.; Lai, J.; Sun, D.; et al. Seamless Lateral Graphene p−n Junctions Formed by Selective in Situ Doping for High-Performance Photodetectors. *Nat. Commun.* **2018**, *9* (1), 5168.

(8) Pi, L.; Wang, P.; Liang, S.-J.; Luo, P.; Wang, H.; Li, D.; Li, Z.; Chen, P.; Zhou, X.; Miao, F.; Zhai, T. Broadband Convolutional Processing Using Band-Alignment-Tunable Heterostructures. *Nat. Electron.* **2022**, *5* (4), 248−254.

(9) Chen, Z.; Zhang, Z.; Biscaras, J.; Shukla, A. A High Performance Self-Driven Photodetector Based on a Graphene/InSe/MoS_2 Vertical Heterostructure. *J. Mater. Chem. C* **2018**, *6* (45), 12407−12412.

(10) Wu, Z.; Peng, J.; Zheng, H.; Li, J.; Lin, Y.; Dong, H.; Fan, J.; Zheng, Z.; Li, W. Ultra-Sensitive Optoelectronics Enabled by Atomically Tailored Interfaces Engineering for Advanced Perceptual Imaging. *Adv. Mater.* **2025**, *37* (35), 2507636.

(11) Guo, T.; Pan, Z.; Li, J.; Sa, Z.; Wang, X.; Shen, Y.; Yang, J.; Chen, C.; Zhao, T.; Li, Z.; Chen, X.; Yang, Z.; Zhu, G.; Huo, N.; Song, X.; Zhang, S.; Zeng, H. Reconfigurable Phototransistors Driven by Gate-Dependent Carrier Modulation in WSe_2/Ta_2NiSe_5 van der Waals Heterojunctions. *ACS Nano* **2025**, *19* (1), 1302−1315.

(12) Ali, F.; Ajmal, H. M. S.; Khan, W. Self-Powered Photo-Thermo Electrochemical Sensor for Harvesting of Low Photo Thermal Energy. *Energy Sources Part A* **2025**, *47* (1), 3953−3965.

(13) Liu, L.; Zhang, X.; Zhang, Q.; Zhang, M.; Zhang, X.; Zhang, P.; Zhao, C.; Gan, X. Reconfigurable Logic of Multidimensional Encryption Based on $ReSe_2$ Homojunction Photodetector. *ACS Nano* **2025**, *19* (27), 25490−25500.

(14) Liu, X.; Qu, D.; Ryu, J.; Ahmed, F.; Yang, Z.; Lee, D.; Yoo, W. J. P-Type Polar Transition of Chemically Doped Multilayer MoS_2 Transistor. *Adv. Mater.* **2016**, *28* (12), 2345−2351.

(15) Wu, E.; Xie, Y.; Zhang, J.; Zhang, H.; Hu, X.; Liu, J.; Zhou, C.; Zhang, D. Dynamically Controllable Polarity Modulation of $MoTe_2$ Field-Effect Transistors through Ultraviolet Light and Electrostatic Activation. *Sci. Adv.* **2019**, *5* (5), No. eaav3430.

(16) Weng, J.; Zhang, Z.; He, T.; Zhang, L.; Zhou, Y.; Xu, T.; Xu, H.; Zhong, F.; Wang, P.; Hu, W. WSe_2 pn Homojunction Photodetector Engineered by In Situ Ferroelectric Doping. *Adv. Funct. Mater.* **2025**, *35* (43), 2506469.

(17) Hu, Y.; Wang, J.; Tamtaji, M.; Feng, Y.; Tang, T. W.; Amjadian, M.; Kang, T.; Xu, M.; Shi, X.; Zhao, D.; Mi, Y.; Luo, Z.; An, L. Integrated Pristine van der Waals Homojunctions for Self-Powered Image Sensors. *Adv. Mater.* **2025**, *37* (23), 2404013.

(18) Ma, T.; Wang, Y.; Feng, G.; Shu, H.; Zhang, J.; Zhou, Y.; Zhou, D.; Lin, Y. Nonvolatile Homogeneous InSe Transistors Regulated by Substrate Engineering. *ACS Nano* **2025**, *19* (34), 31126−31134.

(19) Huo, N.; Konstantatos, G. Ultrasensitive All-2D MoS_2 Phototransistors Enabled by an out-of-Plane MoS_2 p−n Homojunction. *Nat. Commun.* **2017**, *8* (1), 572.

(20) Liu, Y.; Cai, Y.; Zhang, G.; Zhang, Y.; Ang, K. Al-Doped Black Phosphorus p−n Homojunction Diode for High Performance Photovoltaic. *Adv. Funct. Mater.* **2017**, *27* (7), 1604638.

(21) Zhao, B.; Zhang, Z.; Xu, J.; Guo, D.; Gu, T.; He, G.; Lu, P.; He, K.; Li, J.; Chen, Z.; Ren, Q.; Miao, L.; Lu, J.; Ni, Z.; Duan, X.; Duan, X. Gate-Driven Band Modulation Hyperdoping for High-Performance p-Type 2D Semiconductor Transistors. *Science* **2025**, *388* (6752), 1183−1188.
(22) Wang, Y.; Gao, X.; Yang, K.; Gu, P.; Lu, X.; Zhang, S.; Gao, Y.; Ren, N.; Dong, B.; Jiang, Y.; Watanabe, K.; Taniguchi, T.; Kang, J.; Lou, W.; Mao, J.; Liu, J.; Ye, Y.; Han, Z.; Chang, K.; Zhang, J.; Zhang, Z. Quantum Hall Phase in Graphene Engineered by Interfacial Charge Coupling. *Nat. Nanotechnol.* **2022**, *17* (12), 1272−1279.
(23) Lu, X.; Zhang, S.; Wang, Y.; Gao, X.; Yang, K.; Guo, Z.; Gao, Y.; Ye, Y.; Han, Z.; Liu, J. Synergistic Correlated States and Nontrivial Topology in Coupled Graphene-Insulator Heterostructures. *Nat. Commun.* **2023**, *14* (1), 5550.
(24) Duan, S.; Qin, F.; Chen, P.; Yang, X.; Qiu, C.; Huang, J.; Liu, G.; Li, Z.; Bi, X.; Meng, F.; Xi, X.; Yao, J.; Ideue, T.; Lian, B.; Iwasa, Y.; Yuan, H. Berry Curvature Dipole Generation and Helicity-to-Spin Conversion at Symmetry-Mismatched Heterointerfaces. *Nat. Nanotechnol.* **2023**, *18* (8), 867−874.
(25) Zhang, Z.; Zobelli, A.; Gao, C.; Cheng, Y.; Zhang, J.; Caillaux, J.; Qiu, L.; Li, S.; Cattelan, M.; Kandyba, V.; et al. Rotation Symmetry Mismatch and Interlayer Hybridization in MoS_2-Black Phosphorus van der Waals Heterostructures. *Nat. Commun.* **2025**, *16* (1), 763.
(26) Xu, J.; Wang, Z.; Yu, K.; Zhou, G.; Xiao, N.; Wang, K.; Barinov, A.; Marsi, M.; Xiang, H.; Zhang, Z.; et al. Photovoltaic Polarity-Switching Optoelectronic Device Based on MoS_2/TiS_3 Heterostructures for Multifunctional Operation. *Adv. Funct. Mater.* **2025**, No. e15145.
(27) Zheng, S.; Sun, Y.; Shen, Y.; Du, S.; Chen, H.; Jing, Y.; Yuan, Y.; Yao, F.; Li, H.; Liu, X.; et al. Anomalous Reconfigurable-Transport in MoS_2 Transistors by Electrically-Switchable van der Waals Interfacial Dipole. *Adv. Mater.* **2025**, *37* (45), No. e02784.
(28) Miao, N.; Xu, B.; Zhu, L.; Zhou, J.; Sun, Z. 2D Intrinsic Ferromagnets from van der Waals Antiferromagnets. *J. Am. Chem. Soc.* **2018**, *140* (7), 2417−2420.
(29) Zhang, T.; Wang, Y.; Li, H.; Zhong, F.; Shi, J.; Wu, M.; Sun, Z.; Shen, W.; Wei, B.; Hu, W.; Liu, X.; Huang, L.; Hu, C.; Wang, Z.; Jiang, C.; Yang, S.; Zhang, Q.; Qu, Z. Magnetism and Optical Anisotropy in van der Waals Antiferromagnetic Insulator CrOCl. *ACS Nano* **2019**, *13* (10), 11353−11362.
(30) Guo, Y.; Li, J.; Zhan, X.; Wang, C.; Li, M.; Zhang, B.; Wang, Z.; Liu, Y.; Yang, K.; Wang, H.; Li, W.; Gu, P.; Luo, Z.; Liu, Y.; Liu, P.; Chen, B.; Watanabe, K.; Taniguchi, T.; Chen, X.-Q.; Qin, C.; Chen, J.; Sun, D.; Zhang, J.; Wang, R.; Liu, J.; Ye, Y.; Li, X.; Hou, Y.; Zhou, W.; Wang, H.; Han, Z. Van der Waals Polarity-Engineered 3D Integration of 2D Complementary Logic. *Nature* **2024**, *630* (8016), 346−352.
(31) Zheng, X.; Wei, Y.; Zhang, X.; Wei, Z.; Luo, W.; Guo, X.; Liu, J.; Peng, G.; Cai, W.; Huang, H.; et al. Symmetry Engineering Induced In-Plane Polarization in MoS_2 through van der Waals Interlayer Coupling. *Adv. Funct. Mater.* **2022**, *32* (28), 2202658.
(32) Zheng, M.; Liu, J.; Luo, C.; Ge, Y.; Cao, Y.; Huang, C.; Yang, J.; Luo, S.; Cheng, T.; Lin, M.; et al. Synergistic Bridgeable Charge Transfer for Photoluminescence Modulation in Wedding-Cake-Like MoS_2/CrOCl Heterostructures. *Adv. Opt. Mater.* **2025**, *13* (14), 2403492.
(33) Cong, X.; Liu, X.-L.; Lin, M.-L.; Tan, P.-H. Application of Raman Spectroscopy to Probe Fundamental Properties of Two-Dimensional Materials. *Npj 2D Mater. Appl.* **2020**, *4* (1), 13.
(34) Iqbal, M. W.; Shahzad, K.; Akbar, R.; Hussain, G. A Review on Raman Finger Prints of Doping and Strain Effect in TMDCs. *Microelectron. Eng.* **2020**, *219*, 111152.
(35) Hong, J.; Hu, Z.; Probert, M.; Li, K.; Lv, D.; Yang, X.; Gu, L.; Mao, N.; Feng, Q.; Xie, L.; Zhang, J.; Wu, D.; Zhang, Z.; Jin, C.; Ji, W.; Zhang, X.; Yuan, J.; Zhang, Z. Exploring Atomic Defects in Molybdenum Disulphide Monolayers. *Nat. Commun.* **2015**, *6* (1), 6293.
(36) Jang, J.; Kim, Y.; Chee, S.-S.; Kim, H.; Whang, D.; Kim, G.-H.; Yun, S. J. Clean Interface Contact Using a ZnO Interlayer for Low-Contact-Resistance MoS_2 Transistors. *ACS Appl. Mater. Interfaces* **2020**, *12* (4), 5031−5039.
(37) Cao, S.; Zheng, R.; Wang, C.; Ma, N.; Chen, M.; Song, Y.; Feng, Y.; Hao, T.; Zhang, Y.; Wang, Y.; et al. Magnetic-Electrical Synergetic Control of Non-Volatile States in Bilayer Graphene-CrOCl Heterostructures. *Adv. Mater.* **2025**, *37* (3), 2411300.
(38) Peng, Z.-X.; Li, B.-X.; Deng, C.-S. Ultrahigh-Q Fano Resonance in a Cavity-Waveguide Coupled System Based on Second-Order Topological Photonic Crystals with Elliptical Holes. *Opt. Laser Technol.* **2025**, *181*, 111617.
(39) Guan, Y.; Ding, Y.; Fang, Y.; Li, J.; Liu, Y.; Wang, R.; Hao, J.; Xie, H.; Xu, C.; Zhen, L.; et al. Far-Field Femtosecond Laser-Driven $\lambda/73$ Super-Resolution Fabrication of 2D van der Waals $NbOI_2$ Nanostructures in Ambient Air. *Nat. Commun.* **2025**, *16* (1), 4149.
(40) Gan, W.; Ming, L.; Zhang, C.; Peng, G.; Cao, Z.; Chen, Z.; Li, Y.; Wu, C.; Liu, X.; Song, L. Self-Powered Broadband UV-NIR Polarization-Sensitive Photodetector Based on Unipolar van der Waals Heterostructure. *ACS Appl. Mater. Interfaces* **2025**, *17* (23), 34086−34095.
(41) Ding, E.-X.; Karakassides, A.; Zhou, Y.; Fang, R.; Ali, F.; Kauppinen, E. I.; Sun, Z.; Lipsanen, H. High-Performance, Self-Powered Photodetectors Based on Vertically Stacked van der Waals Heterostructures toward Bifacial Photovoltaics. *Nano Energy* **2025**, *140*, 111062.
(42) Zhang, S.; Ye, Y.; Li, H.; Kan, X.; Wang, S.; Sun, S.; Han, T.; Li, F.; Shan, L.; Long, M. High-Sensitive Ultrabroad Photodetector Based on $PtSe_2/WSe_2/PtSe_2$ van der Waals Heterostructure. *Adv. Opt. Mater.* **2025**, *13* (16), 2500127.
(43) Wang, S.; Wang, X.; Wang, W.; Han, T.; Li, F.; Shan, L.; Long, M. Unipolar Barrier Photodetectors Based on van der Waals Heterostructure with Ultra-High Light On/Off Ratio and Fast Speed. *Adv. Sci.* **2025**, *12* (8), 2413844.
(44) Wu, F.; Li, Q.; Wang, P.; Xia, H.; Wang, Z.; Wang, Y.; Luo, M.; Chen, L.; Chen, F.; Miao, J.; et al. High Efficiency and Fast van der Waals Hetero-Photodiodes with a Unilateral Depletion Region. *Nat. Commun.* **2019**, *10* (1), 4663.
(45) Tan, C.; Wang, H.; Zhu, X.; Gao, W.; Li, H.; Chen, J.; Li, G.; Chen, L.; Xu, J.; Hu, X.; Li, L.; Zhai, T. A Self-Powered Photovoltaic Photodetector Based on a Lateral WSe_2-WSe_2 Homojunction. *ACS Appl. Mater. Interfaces* **2020**, *12* (40), 44934−44942.
(46) Varghese, A.; Saha, D.; Thakar, K.; Jindal, V.; Ghosh, S.; Medhekar, N. V.; Ghosh, S.; Lodha, S. Near-Direct Bandgap WSe_2/ReS_2 Type-II p−n Heterojunction for Enhanced Ultrafast Photodetection and High-Performance Photovoltaics. *Nano Lett.* **2020**, *20* (3), 1707−1717.
(47) Tang, Y.; Wang, Z.; Wang, P.; Wu, F.; Wang, Y.; Chen, Y.; Wang, H.; Peng, M.; Shan, C.; Zhu, Z.; et al. WSe_2 Photovoltaic Device Based on Intramolecular p−n Junction. *Small* **2019**, *15* (12), 1805545.
(48) Park, C.; Duong, N. T.; Bang, S.; Nguyen, D. A.; Oh, H. M.; Jeong, M. S. Photovoltaic Effect in a Few-Layer ReS_2/WSe_2 Heterostructure. *Nanoscale* **2018**, *10* (43), 20306−20312.
(49) Jiang, Y.; Wang, R.; Li, X.; Ma, Z.; Li, L.; Su, J.; Yan, Y.; Song, X.; Xia, C. Photovoltaic Field-Effect Photodiodes Based on Double van der Waals Heterojunctions. *ACS Nano* **2021**, *15* (9), 14295−14304.
(50) Wang, X.; Wang, S.; Wu, Y.; Wang, W.; Cao, Z.; Wei, B.; Han, T.; Li, F.; Wang, S.; Shan, L.; et al. A Self-Powered Photodetector Based on Graphene Enhanced $WSe_2/PtSe_2$ Heterodiode with Fast Speed and Broadband Response. *Adv. Opt. Mater.* **2024**, *12* (18), 2400052.
(51) Wong, J.; Jariwala, D.; Tagliabue, G.; Tat, K.; Davoyan, A. R.; Sherrott, M. C.; Atwater, H. A. High Photovoltaic Quantum Efficiency in Ultrathin van der Waals Heterostructures. *ACS Nano* **2017**, *11* (7), 7230−7240.
(52) Kang, Y.; Pei, Y.; He, D.; Xu, H.; Ma, M.; Yan, J.; Jiang, C.; Li, W.; Xiao, X. Spatially Selective P-Type Doping for Constructing Lateral WS_2 p-n Homojunction via Low-Energy Nitrogen Ion Implantation. *Light Sci. Appl.* **2024**, *13* (1), 127.

https://doi.org/10.1021/acsnano.5c18507
ACS Nano 2026, 20, 5034−5043

(53) Wang, F.; Yin, L.; Wang, Z. X.; Xu, K.; Wang, F. M.; Shifa, T. A.; Huang, Y.; Jiang, C.; He, J. Configuration-Dependent Electrically Tunable van der Waals Heterostructures Based on $MoTe_2/MoS_2$. *Adv. Funct. Mater.* **2016**, *26* (30), 5499−5506.
(54) Shin, H.; Taqi, M.; Ali, F.; Lee, S.; Choi, M. S.; Kim, C.; Lee, B.; Liu, X.; Sun, J.; Oh, B.; et al. Self-Powered 2D $MoS_2/WO_x/WSe_2$ Heterojunction Photodetector Realized by Oxygen Plasma Treatment. *Adv. Mater. Interfaces* **2022**, *9* (32), 2201785.
(55) Ouyang, Y.; Zhang, C.; Wang, J.; Guo, Z.; Wang, Z.; Dong, M. Gate-Tunable Dual-Mode Optoelectronic Device for Self-Powered Photodetector and Optoelectronic Synapse. *Adv. Sci.* **2025**, *12* (17), 2416259.
(56) Pei, Y.; Kang, Y.; Zhou, X.; Ma, M.; Yang, M.; He, D.; Li, W.; Xiao, X. Strain-Modulated Dominant Response Band of Self-Powered Photodetector Based on WSe_2 Lateral p−n Homojunction. *Small* **2025**, *21* (7), 2410773.
(57) Gao, B.; Yan, Y.; Zhang, S.; Wu, Z.; Meng, Y.; Zhang, Y.; Wang, W.; Shen, Y.; Hu, S.; Li, B.; et al. Precise p-Type Substitutional Doping Enables WS_2 p-n Anti-Ambipolar Homojunction Phototransistor Arrays. *Adv. Funct. Mater.* **2025**, *35* (33), 2425884.
(58) Perdew, J. P.; Burke, K.; Ernzerhof, M. Generalized Gradient Approximation Made Simple. *Phys. Rev. Lett.* **1996**, *77* (18), 3865−3868.
(59) Liechtenstein, A. I.; Anisimov, V. I.; Zaanen, J. Density-Functional Theory and Strong Interactions: Orbital Ordering in Mott-Hubbard Insulators. *Phys. Rev. B* **1995**, *52* (8), R5467−R5470.
(60) Chadi, D. J. Special Points for Brillouin-Zone Integrations. *Phys. Rev. B* **1977**, *16* (4), 1746−1747.
(61) Grimme, S.; Antony, J.; Ehrlich, S.; Krieg, H. A Consistent and Accurate Ab Initio Parametrization of Density Functional Dispersion Correction (DFT-D) for the 94 Elements H-Pu. *J. Chem. Phys.* **2010**, *132* (15), 154104.

https://doi.org/10.1021/acsnano.5c18507
ACS Nano 2026, 20, 5034−5043